Homologous Confined Filament Eruptions via Magnetic Breakout

C. Richard DeVore[1] and Spiro K. Antiochos[2]
Naval Research Laboratory, Washington DC 20375, USA

Short Title

Homologous Confined Filament Eruptions

Abstract

We describe magnetohydrodynamic simulations of a bipolar active region embedded in the Sun's global background field and subjected to twisting footpoint displacements concentrated near its polarity inversion lines to produce strong magnetic shear. The dipole moments of the active region and background field are antiparallel, so that the initially potential magnetic field contains a coronal null. This configuration supports magnetic breakout eruptions in our simulations that exhibit three novel features. First, the eruptions are multiple and homologous: the flare reconnection following each eruption reforms the magnetic null, setting the stage for a subsequent episode of breakout reconnection and eruption driven by the ongoing footpoint motions. Second, the eruptions are confined, that is, their rapidly rising, moderately sheared field lines do not escape the Sun but instead come to rest in the outer corona, comprising a large coronal loop formed by reconnection during the rise phase. Third, the most strongly sheared field lines of the active region are quite flat prior to eruption, expand upward sharply during the event, and lose most of their shear through reconnection with overlying flux, while lower-lying field lines survive the eruption and recover their flat configuration within a few hours. These behaviors are consistent with filament disappearance followed by reformation in place. We also find that the upward motion of the erupting sheared flux exhibits a distinct three-phase acceleration profile. All of these features of our simulations – homology, confinement, reformation, and multiphase acceleration – are well established aspects of solar eruptions.

Subject Headings

Sun: coronal mass ejections – Sun: filaments – Sun: flares – Sun: magnetic fields – magnetohydrodynamics

[1] Laboratory for Computational Physics and Fluid Dynamics; devore@lcp.nrl.navy.mil
[2] now at Space Weather Laboratory, NASA Goddard Space Flight Center, Greenbelt MD 20771, USA

1. INTRODUCTION

The Sun displays a variety of eruptive behaviors from multiple types of source regions at its surface. At the largest scales, these events eject enormous amounts of magnetic flux and plasma into interplanetary space at high speeds (a coronal mass ejection, or CME) and emit copious quantities of high-energy particles and radiation (a solar flare) (e.g., Crooker et al. 1997; Song et al. 2001; Gopalswamy et al. 2006; Kunow et al. 2006). At smaller scales, an event may disrupt the participating plasma structure without ejecting matter completely out of the corona in a CME. In the latter case the eruption is referred to as confined, as contrasted with ejective in the former. A quite general property of the source regions of solar eruptions is the presence of strongly non-potential, or electrical current-carrying, magnetic fields. Such fields contain excess ('free') magnetic energy, above the potential-state minimum energy, that can be tapped to power the eruption. They also frequently support either cold filament or hot X-ray sigmoid plasma – sometimes both at different altitudes – within the ambient corona. Events that disrupt or eject these structures sometimes are followed by the reformation in place of the filament or sigmoid. Within this class, a few source regions exhibit sequences of two or more similar eruptions occurring only hours to a day or so apart. Such events are said to be homologous.

A number of theories have been developed to account for solar eruptions (for reviews, see Forbes 2000; Klimchuk 2001; Lin et al. 2003; Forbes et al. 2006; Mikić & Lee 2006). We have developed and continue to explore the consequences of the magnetic breakout model (Antiochos 1998; Antiochos et al. 1999; MacNeice et al. 2004; Phillips et al. 2005; DeVore & Antiochos 2005; Lynch et al. 2005). Breakout exploits a vulnerability of multipolar configurations, which consist of two or more distinct flux systems separated by null points ($\boldsymbol{B}$=0) in the corona, to rearrangements of the magnetic field's connectivity. Reconnection across the current sheet at a stressed null reconfigures the field geometry, enabling restraining overlying field lines to be converted into nonrestraining field lines of neighboring flux systems. This removal of the magnetic tethers holding down the filament or sigmoid of the source region eventually can run away, leading to an explosive disruption as the stored magnetic free energy is converted to kinetic, gravitational, and thermal energy of the entrained plasma. If the available energy is sufficient, the process can produce a CME and its associated flare.

In this paper, we describe the results of our recent simulations of breakout-induced eruption from a model bipolar active region embedded in the bipolar background field of the Sun. The initially potential coronal magnetic field is energized by imposing line-tied footpoint motions that follow the surface contours of the radial field B_r in a clockwise direction, within both polarities of the active region and concentrated near its polarity inversion lines. We find that the accumulating magnetic stresses and free energy power a sequence of three similar confined eruptions over the duration of the simulation. In each eruption, a first phase of very gradual upward lifting of the sheared flux is driven by the slow energizing footpoint motions; it culminates in the onset of fast breakout reconnection at the stressed null. There follows a second phase of strong outward acceleration of the sheared flux, as it undergoes an ideal magnetohydrodynamic (MHD) expansion into the volume vacated by the retracting, breakout-reconnected field lines above. The rising flux is unable to escape the Sun fully, however, instead coming to rest in the high corona and forming a large, transequatorial loop. This third phase of strong radial deceleration of the flux is accompanied by the onset of flare reconnection below the sheared flux, which rather quickly reforms the coronal null, the filament or sigmoid field adjacent to the surface, and the oppositely directed polar field overhead. The breakout configuration is thereby fully restored at the conclusion of each event, so that the stage is set for the next eruption to follow in the sequence. Thus, our simulations show that the breakout model can account for the occurrence of homologous, confined filament eruptions with reformation of the participating structure and a multiphase acceleration profile. Three of these features – homology, confinement, and reformation – are shown here to be consequences of magnetic breakout for the first time. So far as we are aware, this also is the first self-consistent demonstration of homology and reformation in any simulated eruption in a fully three-dimensional configuration.

2. MODEL

The numerical simulations were performed with *ARMS*, the *A*daptively *R*efined *M*agnetohydrodynamics *S*olver. *ARMS* integrates the time-dependent, three-dimensional, MHD equations on block-adaptive meshes tailored to the problem being solved. For this study, we formulated the MHD equations on a spherical (r,θ,φ) grid as follows:

$$\begin{aligned}
\frac{\partial \rho}{\partial t} + \nabla \bullet \rho \mathbf{v} &= 0 \\
\frac{\partial \rho \mathbf{v}}{\partial t} + \nabla \bullet \rho \mathbf{v}\mathbf{v} &= -\nabla P + \frac{1}{4\pi}\left(\nabla \times \mathbf{B}\right) \times \mathbf{B} + \rho \mathbf{g} \\
\frac{\partial T}{\partial t} + \nabla \bullet T\mathbf{v} &= \left(2-\gamma\right) T \nabla \bullet \mathbf{v} \\
\frac{\partial \mathbf{B}}{\partial t} - \nabla \times \left(\mathbf{v} \times \mathbf{B}\right) &= 0
\end{aligned} \tag{1}$$

All of the symbols have their standard meanings. We assumed an ideal hydrogen-plasma equation of state whose ratio of specific heats γ = 5/3 and used the solar gravitational acceleration $\mathbf{g} = -GM_{\odot}\mathbf{r}/r^3$. The temperature equation describes simple adiabatic heating or cooling of the plasma as it compresses or expands, respectively. There are necessary, stabilizing numerical diffusion terms implicit in all of these equations. Those in the induction equation permit magnetic reconnection to occur at current sheets that steepen to attain the finite scale of the simulation grid.

The initial atmosphere combines a spherically symmetric plasma in hydrostatic pressure balance with a potential magnetic field, so that it is in mechanical and thermal equilibrium. The coronal temperature profile was specified as

$$T_0\left(r\right) = T_{\odot}\left(r/R_{\odot}\right)^5 \left[\left(R_c/R_{\odot}\right)^6 + 1\right] / \left[\left(R_c/R_{\odot}\right)^6 + \left(r/R_{\odot}\right)^6\right], \tag{2}$$

which rises from its surface value, attains a maximum, and then declines thereafter with an inverse-r falloff at large radii. The latter produces an inverse-r^s falloff of the plasma pressure, which for s=6 maintains an approximately uniform (small) ratio of plasma to magnetic pressure in the dominant dipole component of the magnetic field far from the Sun. We solved the radial force balance condition between pressure and gravity exactly on the finest grid accessible to the simulation. On coarser grids, the solution is injected conservatively from the next finer level, to preserve the total mass and internal energy in the eight fine cells that comprise each coarse cell and to maintain pressure balance across any horizontal jumps in the grid refinement level.

For the background field, we chose an axisymmetric surface distribution concentrated toward the poles that reproduces the Wilcox Solar Observatory's line-of-sight measured field (in G),

$$B_r\left(R_{\odot},\theta,\varphi\right) = +1\cos\theta - 5\cos^3\theta + 12\cos^5\theta - 3\cos^7\theta\,. \tag{3}$$

This radial field is antisymmetric across the equator and reaches its peak strength of 5 G at the poles. It is drawn in Figure 1 (*solid* curve), along with its line-of-sight projection (*dashed* curve) and discrete values from WSO measurements (Duvall et al. 1979; *filled circles*). We modeled our bipolar active region as a circular patch of magnetic flux centered on the intersection of the equator and the central meridian and bisected by an internal polarity inversion line (PIL) that coincides with the equator. The field profile was specified to be

$$B_r\left(R_\odot,\theta,\varphi\right)=B_0\,\mathrm{sgn}\left(\chi\right)\left|\chi/\psi_0\right|^{1/4}\left[1-\left(\chi/\psi_0\right)^2-\left(\varphi/\psi_0\right)^2\right]^{1/4}, \tag{4}$$

where $\chi = \pi/2-\theta$ is the latitude and ψ_0 is the half-angle extent of the patch in both latitude and longitude. The exponent ¼ concentrates strong field relatively close to the PIL, as is observed in many active regions and which facilitates the accumulation of magnetic free energy as shearing footpoint motions are imposed on those near-PIL field lines. Figure 2 shows the resultant total (active region plus background) magnetic field values (*filled circles*) versus latitude at the central meridian (*left*) and versus longitude at the latitude of peak strength in the south (*right*) at the discrete points of the simulation grid.

We constructed a pattern of imposed surface flows from the prescription

$$\mathbf{v}\left(R_\odot,\theta,\varphi\right)=v_0\left[1-\cos\left(\pi\left[B_r\left(R_\odot,\theta,\varphi\right)-B_1\right]/\left[B_2-B_1\right]\right)\right]\hat{\mathbf{r}}\times\nabla_t B_r\left(R_\odot,\theta,\varphi\right), \tag{5}$$

where ∇_t is the gradient operator tangential to the surface. The flows are restricted to regions where the radial field B_r ranges between B_1 and B_2, where B_2 is near the extremal values at which $\nabla_t B_r$ vanishes in the active region. Outside of that range, the flows are set to zero. The resultant circulation pattern preserves the surface contours of B_r throughout the simulation. This idealization is convenient, because it means that the minimum magnetic energy of our configuration is fixed throughout the simulation, and is equal to the energy of the initial potential field. Spatial profiles (*open circles*) of longitudinal velocity versus latitude at central meridian (*left*) and of colatitudinal velocity versus longitude at the latitude of peak field strength in the south (*right*) are shown in Figure 2. During an initial startup phase, we also include a multiplicative temporal factor

$$f(t)=\left[1-\cos\left(\pi t/\tau\right)\right]/2 \tag{6}$$

that smoothly accelerates the flows from rest at time $t = 0$ to terminal velocity at time $t = \tau$.

For the calculations shown in this paper, we used the following values of the parameters:

$$\begin{gathered} T_\odot=4\times10^5\ \mathrm{K},\ R_c=1.25R_\odot,\ P_\odot=1\times10^{-1}\ \mathrm{dyn\ cm^{-2}};\\ B_0=5\ \mathrm{G},\ 2\psi_0=\pi/4=45^\circ;\\ B_1=\pm2.4\ \mathrm{G},\ B_2=\pm3.2\ \mathrm{G},\ v_0=\pm9.3\times10^{15}\ \mathrm{cm^2\ s^{-1}\ G^{-1}},\ \tau=1\times10^4\mathrm{s}. \end{gathered} \tag{7}$$

The atmosphere parameters yield a typical spherically symmetric, hydrostatic coronal plasma. Its temperature rises from 4×10^5 K at 1 $R_\odot$ to 1×10^6 K at 1.65 $R_\odot$, then falls off to just over 1.5×10^5 K at 13 $R_\odot$. Our model active region contains a nominal amount of magnetic flux, 3.4×10^{21} Mx of each polarity, compared to those observed. However, its peak field strength of 5 G is low, and its area coverage is correspondingly large. These choices are more typical of aged, dispersed active regions than of young, compact ones. We adopted them for numerical convenience, since they yield moderate values of the Alfvén speed (360 km s^{-1}), magnetic pressure (2 dyn cm^{-2}), and plasma beta (ratio of plasma to magnetic pressures; 5%) at low altitudes in our simulation. They also impose manageable demands on the grid spacing required to resolve the region and its internal flows and the timestepping needed to maintain numerical stability. More realistic values for the field strength and area necessarily would make such simulations even more computationally intensive than those reported here, and will be reserved for future investigations. The positive (negative) values of the flow coefficients are used in the positive (negative) magnetic polarity of the active region. Our resultant imposed surface flows have a peak speed of 20 km s^{-1}, which is both subsonic and sub-Alfvénic, although faster than typically observed photospheric shearing and twisting flows. This too is for numerical convenience.

The computational domain extends from 1 $R_\odot$ to 13 $R_\odot$ in radius and over 7π/8 radians in both latitude and longitude, with the grid linearly spaced in all three directions. The latitudinal range excludes small cones at the poles where the grid lines converge. All boundaries are closed and reflecting to normal flows, i.e. $v_n = 0$, and all boundaries except the bottom radial boundary also are no-slip, i.e. $\mathbf{v}_t = 0$. We have found that our simulation results are insensitive to the positions of the outer radial and the four angle boundaries. A preceding simulation used a domain extending to only 5 $R_\odot$ and over just 3π/4 radians; a succeeding simulation on an exponentially spaced radial grid extended to 50 $R_\odot$ and covered 7π/8 radians. The qualitative features are identical among the three cases, each of which produces a confined eruption prior to time $t = 3\times10^4$ s, when we halted the two comparison runs. The quantitative differences among the three simulations are very modest. We used four grid levels in each calculation. The finest grid level for the simulations shown in this paper corresponds to a $1920\times448\times448$ uniform grid over the entire domain, which would require a third of a billion grid points with 4 Mm of linear resolution and 0.4º of angle resolution. The adaptive mesh actually used employs fewer than six million grid points, however, saving a factor of 64 in memory and arithmetic operations.

The initial magnetic configuration, the adapted grid, and the imposed flow pattern are illustrated in Figure 3, in a global view from the solar east limb (*top left*), a closeup view of the bipolar region from the southeast quadrant (*top right*), and a view from above (*bottom*). The Sun's surface (r slice) is rendered in all panels, and the central meridian plane (φ slice) in the top panels. The color shading shows the magnitude and sign (positive in *blue*, negative in *red*) of the radial magnetic field B_r, and the straight lines (*black*) are the boundaries of grid blocks consisting of $8\times8\times8$ cells on those surfaces. The clockwise pattern of circulating footpoint motions is indicated by the arrowheads (*white*) on the solar surface, and by streamlines (*white*) in the view from above. Selected magnetic field lines are drawn as thick traces, color-coded according to the flux system to which they belong: the inner equatorial fields (*blue*); the outer polar fields (*red*); and the midlatitude side arcade fields (north: *green*; south: *yellow*). All but two of these field lines are drawn from fixed positions on the solar surface outside of the zones of imposed footpoint motions, and so retain their identities throughout the simulation; the exceptions are the outermost blue and innermost red lines marking the location of the magnetic null. This initial state is a fully three-dimensional breakout configuration with four distinct flux systems, analogous to the axisymmetric configurations assumed in our earlier studies (Antiochos et al. 1999; MacNeice et al. 2004; Phillips et al. 2005; DeVore & Antiochos 2005). Whereas in those cases a magnetic null line positioned above the equator completely encircled the Sun, here the null line has an apex centered above the active region and descends from that point to reach the solar surface at the crossings of the equatorial and the circular active-region PILs that separate the four polarity regions. In our field-line figures below, we use additional colors to mark those lines in the equatorial system whose footpoints are moved during the simulation and so belong to the sheared filament or sigmoid (*magenta*), and those in the polar system that comprise the transequatorial loops newly formed during the eruption (*cyan*), as described later. The imposed footpoint motions introduce magnetic shear into the central, equatorial arcade and also into both midlatitude arcades at the sides. This shear energizes all three of those flux systems – the central one most strongly and effectively – as time passes. The flows are concentrated near the PILs of the active region and away from the separatrix field lines connecting through the X-type null, as can be seen in the closeup. At the outset, we required that the adapted grid refine to the maximum level allowed over a spherical wedge 45° across in latitude and longitude and extending from 1 $R_\odot$ to 2.5 $R_\odot$ in radius. This fine-grid region thus fully encloses the active region laterally and accommodates the anticipated vertical expansion of the field during the slow stressing phase, providing maximal resolution of the expected breakout and flare current sheets.

Despite the concentration of grid blocks where the current sheets form, we find that the total energy is not conserved perfectly in the simulation due to our nonconservative formulation of the MHD equations. In particular, modest losses of energy occur during each eruption, when substantial numerical reconnection of magnetic fields takes place across both the breakout and flare current sheets. The associated numerical Joule heating is not captured by an MHD model such as ours, with its adiabatic equation for the plasma temperature, and so is lost from the system. We are working to develop a method that captures this numerical heating locally through a total energy equation, but simultaneously avoids introducing potentially large errors into the plasma

thermal energy, which must be calculated by subtraction. This is quite challenging numerically in a very low-pressure plasma. We anticipate that the energy lost is insufficiently large to make a qualitative change in the principal results below, however, because the magnetic field so dominates the dynamics in our low-beta corona. Its main quantitative effect would be to raise the temperature of the heated plasma adjacent to the current sheets, which is a ubiquitous feature of solar flares.

3. RESULTS

Some key features of our simulation are illustrated by the evolution of the magnetic and kinetic energies of the system, whose values in the initial, hydrostatic equilibrium state are 6.72×10^{31} ergs and zero, respectively. Changes from these initial values are shown in Figure 4. By the end of the acceleration phase of the footpoint motions at time $t = 1.0\times10^4$ s, the magnetic free energy (*solid* curve) has acquired a linear increase with time that persists through most of the remainder of the simulation. The exceptions are three brief intervals of sharp decreases beginning at about times $t = 2.75\times10^4$ s, 4.25×10^4 s, and 6.0×10^4 s, each of which lasts for approximately 2.5×10^3 s, or 45 min. The resultant six extremal points in the free energy curve are marked by thin vertical lines in the figure. These pairs of points mark the initiation and saturation of three successive confined eruptions of the stressed equatorial arcade. The kinetic energy (*dotted* curve) enters a steep rising phase at the first extremal point of each pair and attains a maximum value at the second extremal point. Following its peak, the kinetic energy declines steeply for some time and then more gradually, before bottoming out just prior to the onset of the succeeding event. These short-lived episodes of partial conversion of magnetic to kinetic energy clearly are quasiperiodic, one of several indicators of the homologous character of the eruptions in our configuration.

The quasiperiodic behavior, together with the gradual secular evolution, is illustrated further in the sequence of images of magnetic field lines shown in Figure 5. Both east-limb global views (*left*) and southeast closeups (*right*) are drawn at times following each of the three eruption episodes in the simulation: $t = 3.625\times10^4$ s (*top*), 5.25×10^4 s (*middle*), and 7.0×10^4 s (*bottom*). These times are roughly midway between eruptions #1 and #2, between #2 and #3, and between #3 and an anticipated eruption #4, respectively. The quasiperiodic behavior is clearly evident, specifically in the nearly identically reformed low-coronal null point and its underlying equatorial and overlying polar arcades at each time. This restoration of the magnetic breakout topology in the low corona, essentially identical to that of the initial state shown in Figure 3, sets the stage for each subsequent eruption in the homologous sequence. At the same time, accumulating secular changes also are apparent, particularly the increasing flux contained in and the ever-rising height of the transequatorial loop (*cyan*) in the global views. The transequatorial field lines are drawn at altitude multiples of 0.05 $R_\odot$, or 35 Mm, above the surface at the intersection of the equatorial and central meridional planes. Their accumulation and expansion force the overlying polar fields outward, of course. Less obvious but also noticeable are the midlatitude arcades' increasingly sheared field lines, rooted in the right foreground and left background of the closeup views. The associated stresses cause the midlatitude arcades to expand upward gradually with time as well, along with – but at a slower rate than – the transequatorial-loop and polar fields.

The evolution of the field at closely spaced times during the second of our three homologous eruptions is illustrated in Figure 6. The global (*left*) and closeup (*right*) views are shown at times $t = 4.125\times10^4$ s (*top*), 4.375×10^4 s (*middle*), and 4.625×10^4 s (*bottom*). These times bracket those of maximum and minimum magnetic free energy during the second eruption at about $t = 4.25\times10^4$ s and 4.5×10^4 s, respectively. The global view in the top pair of frames shows clearly the flattening of the breakout current sheet at the null line between the equatorial and polar arcades. Also evident are two high-lying transequatorial-loop field lines that were formed during the first eruption in the sequence. The closeup view shows that the inner sheared-core field (*magenta*) has risen substantially, albeit gradually, since the previous interregnum shown in the top row of the preceding figure. It now reaches to some 210 Mm above the surface, compared to only 105 Mm earlier (these field lines, like those in the transequatorial loop, are drawn at height multiples of 35 Mm). Furthermore, even

quite high lines in the sheared core, such as the (third) one drawn in this figure at a height of 105 Mm, are very flat over their midsections. A model of prominence plasma as a dynamic entity driven by nonuniform heating and radiative condensation (Karpen et al. 2006) suggests that field lines such as these should be able to support spatially narrow, but very elongated, long-lived threads of filament plasma. If true, then our simulation is fully consistent with observed filament eruptions in which a long, slow rise phase precedes the onset of strong acceleration and fast eruption.

The middle pair of frames in Figure 6 shows three key features of the mid-eruption evolution of our system. First, the equatorial arcade overlying the sheared-core flux of the active region strongly distends, reconnects, and then retracts to the sides. Its field lines (*blue*) thus topologically join, and temporarily overlie, the neighboring midlatitude arcades (*green* and *yellow*). This is a consequence of the breakout reconnection across the current sheet at the null high in the corona. Second, the sheared-core flux of the active region (*magenta*) expands strongly radially, and also latitudinally at high altitudes. This follows directly from the catastrophic loss of force balance between the magnetic pressure in the sheared core and the magnetic tension in the now-removed overlying arcade fields. The sheared-core flux also erodes from the outside during its expansion, as it encounters oppositely directed polar field (*red*) above it. This continuation of the breakout process transfers shear from the rising, reconnecting core flux to the neighboring midlatitude arcades. Third, intermingled with the lower-lying, rapidly rising sheared-core field lines are newly formed transequatorial-loop lines (*cyan*). Unlike the former, which are rooted in the two polarities of the active region, the transequatorial-loop field lines are rooted in the background field at high latitudes in both hemispheres. Their origin is explained below.

The bottom pair of frames in Figure 6 shows that these newly formed transequatorial-loop field lines are ejected into the high corona, where they join preexisting similar lines from the prior (first) eruption in our sequence. Note that the intervening sheared-core flux evident in the middle row of the figure has been removed completely by the aforementioned ongoing breakout reconnection with the overlying polar field. Only the new transequatorial-loop field lines (*cyan*) survive the transit into the high corona, carrying their substantial shear with them. A relatively small amount of sheared-core flux (*magenta*) is left behind in the low corona. Between these two groups of field lines, the previously breakout-reconnected equatorial arcade fields (*blue*) have relaxed back together, forming a vertical current sheet extending along the equator. At this time, much of their flux already has reconnected to reform a nearly potential arcade in the low corona, below the reestablished magnetic null across which the reconnection continues. This flare reconnection is common to nearly all models of solar eruptions, and is essentially universally accepted as the driving agent behind the familiar flare loops and ribbons. Although only much more moderately sheared-core field lines survive the eruption compared to those present at event onset, these low-lying remnant lines acquire quite flat midsections over a substantial length as a new magnetostatic equilibrium is achieved. Thus, in light of our mention above of the thermal nonequilibrium model of prominences, it is plausible that cold, dense filament plasma might persist on some of these low-lying sheared field lines throughout the eruption, or alternatively could reform on these lines shortly afterward. Such scenarios would correspond to partial filament eruptions, or to full eruptions with prompt reformation of the filament, respectively, both of which are rather routinely observed on the Sun.

The key reconnection processes – breakout and flare – that operate in our eruptions are illustrated by pairs of pre- and post-reconnection magnetic field lines in Figure 7. Each panel shows both a pre-reconnection pair (*lower left*) and a post-reconnection pair (*upper right*), and each field line is color-coded according to the flux system to which it belongs. Breakout reconnection (*top*) starts early in the eruption sequence, across the current sheet at the distorted magnetic null high in the corona. This is illustrated here by unsheared equatorial arcade (*blue*) and overlying polar (*red*) field lines at time $t = 4.125\times10^4$ s (the same lines were drawn previously in Figure 6, *top*). Their reconnection produces new midlatitude arcade field lines in the north (*green*) and south (*yellow*) shown at time $t = 4.25\times10^4$ s (similar lines were drawn later in the evolution in Figure 6, *middle* [*blue*]). As we mentioned above, the breakout reconnection eventually exhausts all of the unsheared equatorial arcade flux and then begins to consume the outer portion of the sheared-core flux rising below it (as represented by the bulb-shaped sheared-core lines in Fig. 6, *middle* [*magenta*]). Therefore, we find that the breakout

reconnection continues well into the second phase of the eruption, when the outward acceleration is maximal and the radial velocity is approaching its peak. Our previous axisymmetric simulations exhibited this behavior as well (MacNeice et al. 2004).

The formation of the new transequatorial-loop field lines also occurs during this second phase, as shown by the mid-eruption panel (*middle*) of Figure 7. The post-reconnection field (*upper right*) at time $t = 4.375 \times 10^4$ s consists of a very long transequatorial-loop line (*cyan*) and a short, moderately sheared line in the active-region core (*magenta*). Their progenitors (*lower left*) at time $t = 4.25 \times 10^4$ s are lines belonging to the north (*green*) and south (*yellow*) midlatitude arcades. These field lines connect each polarity of the active region to the opposite polarity of the background field within the same hemisphere. Initially, these field lines were in a potential state and resided within the active region well away from the equatorial PIL – in the northwest portion of the region in the northern hemisphere, and in the southeast portion in the southern hemisphere. The clockwise rotation of the active-region flux by the imposed footpoint motions eventually transports these lines into the shear zone adjacent to the PIL, where they are rooted in the figure. When all of the sheared flux in the vicinity rises rapidly during the second phase of the eruption, these lines are forced toward the equatorial plane, where they reconnect, by the magnetic pressure of the midlatitude arcades on both sides. The resultant short field line with moderate shear relaxes downward under tension from the reconnection site, while the long line containing most of the shear is free to spring upward, trailing the core field lines of the filament as they escape higher into the corona.

After the rising sheared field lines in the equatorial and midlatitude arcades have been cleared sufficiently from the low corona above the eruption site, the field lines rooted outside of the shear zone begin to relax back toward and to reconnect across the vertical current sheet separating them. Pre-reconnection field lines in this third, late-eruption phase of the event again belong to the north (*green*) and south (*yellow*) midlatitude arcades, but possess little or no shear, as shown in Figure 7 (*bottom*). These field lines are just those formed by breakout reconnection during the first phase of the eruption (Fig. 7, *top*); here they are shown at time $t = 4.5 \times 10^4$ s. After reconnecting across the radially extended current sheet separating them, they repopulate both the equatorial arcade (*blue*) and the overlying polar field (*red*), as shown here by the post-reconnection field lines drawn at time $t = 4.625 \times 10^4$ s. These new lines then relax away – downward and upward, respectively – from the magnetic null (cf. the inner equatorial/polar pair at this time in Fig. 6, *bottom*). Eventually, this ongoing flare reconnection approximately fully restores the pre-event magnetic configuration in the low and middle corona (cf. the near-equilibrium state attained by time $t = 5.25 \times 10^4$ s in Fig. 5, *middle*). The stage is now set for the magnetic free energy injected by the ongoing slow surface motions to power a subsequent eruption very similar to the one just concluded, driving the whole sequence of homologous events.

The breakout and flare reconnection processes just described also are responsible for the final disposition of the magnetic helicity injected by the footpoint motions. We have seen that the motions introduce strong magnetic shear onto field lines of both the equatorial arcade (*magenta* in Figs. 5 and 6) and the midlatitude arcades (*green* and *yellow* in Fig. 7, *middle*). The resultant helicity resident on those low-lying field lines is transferred to high-lying field lines principally during the rapid-ascent phase of the eruption. The sheared-core flux of the equatorial arcade breakout-reconnects with overlying polar flux in the same way as the unsheared flux (Fig. 7, *top*), except that the newly formed midlatitude field lines have a substantial shear on them inherited from their sheared-core progenitor. Meanwhile, the low-lying sheared field lines of the midlatitude arcades suffer the flare-like reconnection already shown explicitly in Figure 7 (*middle*), which transfers their helicity principally to the newly formed transequatorial loops that spring upward into the high corona, leaving a small amount on the now more weakly sheared equatorial arcade lines below. In both processes, the magnetic helicity is transferred from low-lying field lines rooted very near the PIL of the AR on one end or both ends, and is transferred to high-lying field lines rooted far away from the PIL on one end or both ends. This transfer necessarily must occur if helicity is to be conserved during a confined eruption such as ours, in which it is unable to escape the Sun altogether even as it is expelled violently from the immediate vicinity of the PIL.

To understand further the kinematics and dynamics of our eruptions, we have measured the apex positions of selected field lines in the simulation, as shown in Figure 8. Unsheared arcade field lines (*left*) that overlie the sheared-core flux were traced from the surface at the central meridian, at north latitudes 5.5° (*solid* curves), 6.5° (*dotted* curves), and 7.5° (*dashed* curves). These are just the inner three equatorial arcade field lines (*blue*) drawn in Figures 3, 5, and 6. Their apex positions rise rapidly as the peak magnetic free energy is approached just prior to the eruptions. Each apex trajectory terminates when breakout reconnection snaps the arcade field line at high altitude and joins it to the global background field at high north latitudes (cf. Fig. 7, *top*); and the trajectory resumes when flare reconnection later reestablishes the arcade field line across the equator at low altitude (cf. Fig. 7, *bottom*). Note carefully that this arcade reformation begins when the magnetic free energy reaches its minimum, and the kinetic energy already has attained its maximum and is beginning to decline. Thus, the flare reconnection follows, rather than precedes, the strong outward acceleration of the ejecta, as we described previously. Meanwhile, the rapidly rising sheared field lines (*right*) tracked during the eruptions belong either to the active region's sheared-core flux (*solid* curves) or to the transequatorial loops formed during the events (*dotted* and *dashed* curves). Representative examples of these field lines are the central line of the 'light bulb' of sheared-core flux (*magenta*) and the newly formed, low-altitude transequatorial lines (*cyan*) at mid eruption in Figure 6 (*middle*), respectively. The trajectories of the former terminate when they suffer breakout reconnection with the overlying polar field during their rise into the high corona; the trajectories of the latter are initiated at their formation in the low corona by the mid-eruption reconnection process described above. As can be seen in the right panel of Figure 8, after the transequatorial-loop field lines have been brought to rest by the tension of the overlying field lines high in the corona, they relax back down toward the surface. This downward motion is subsequently reversed by the next eruption in the homologous sequence, in which the previously formed transequatorial-loop field lines are pushed still higher in the corona by the newly formed lines rising up from below to join them. Consequently, the apex positions of the transequatorial loops oscillate above 2 $R_\odot$, with a secular increase in time of their extremal altitudes.

Although our simulated eruptions are confined, with the rising transequatorial-loop field lines eventually coming to rest in the high corona, they nevertheless are rather vigorous. Both the sheared-core flux and the transequatorial loop rise about 1 $R_\odot$ in the 2.5×10^3 s separating the free energy extrema. This implies an average radial velocity of about 300 km s^{-1} and an acceleration and deceleration of 450 m s^{-2} in the sheared ejecta. In contrast, the gradual rise of both the overlying equatorial-arcade and sheared-core field lines leading up to eruption onset – about .25 $R_\odot$ in the roughly 1.25×10^4 s between each pair of events – implies an average acceleration of only about 2 m s^{-2}, and a radial velocity late in the shear phase of about 25 km s^{-1}. Thus, we obtain a clear three-phase acceleration profile for our simulated eruption: a long interval of slow acceleration as the core field is energized by the shearing footpoint motions; a short interval of fast acceleration following the completion of the breakout reconnection and accompanied by the formation of the transequatorial-loop fields via flare reconnection of sheared flux; and a short interval of fast deceleration to rest of the rising transequatorial-loop lines accompanied by restoration of the low-lying filament fields and reformation of the overlying breakout configuration due to the flare reconnection of unsheared flux.

The evolution of the magnetic field over the entire duration of our simulation is captured in a video (*DA08.mpg*) that is provided with the electronic version of this paper. Both the global and closeup perspectives of Figures 3, 5, and 6 are shown in successive segments of the movie. For clarity, the newly formed transequatorial-loop field lines (*cyan*) shown in the figures are omitted from the movie. The high frame rate used in the movie accentuates the rapid expulsions of flux during the eruptions, as well as the oscillations of the outer coronal field driven by the accumulating transequatorial-loop flux. Stepping through the movie frame by frame highlights the gradual evolution of the configuration between eruptions.

In the simulation described thus far, an initial interval of smooth acceleration of the footpoint motions from rest was followed by a long interval in which the motions were maintained at a fixed speed through three successive eruptions. This may raise the question whether the ongoing energization of the magnetic field by those motions played a critical role in the occurrence of eruption, i.e., whether the events were at least partially

directly driven by the motions, rather than solely by the conversion of previously stored magnetic free energy. To address this issue, we restarted our simulation at time $t = 3.75\times10^4$ s and decelerated the flows gradually to rest over the ensuing 1×10^4 s, using a cosine time profile like that employed in the startup phase (Eq. 6). The accumulated displacement over this interval is one-half of that of the steady flow, i.e., corresponds to that of our original simulation at time $t = 4.25\times10^4$ s. This was the time of onset of the second of our homologous eruptions (cf. Fig. 4). The resultant energy profiles for the arrested-flow case are shown in Figure 9. The eruption onset (marked by the maximum in the magnetic free energy [*solid* curve]) and its peak (the maximum in the kinetic energy [*dotted* curve]) are somewhat delayed from their times of occurrence in the steady-flow case (thin vertical lines), as expected. Also, the maximum kinetic energy is reduced by about 30% from the value attained under steady flow. Following eruption onset, the system required about 1.25×10^4 s, or about four hours, to relax to a new approximate equilibrium of steady magnetic and kinetic energies. The event released about 1.5×10^{30} ergs of magnetic free energy, which is fully consistent with the offset in the free energy curve following the second eruption in Figure 4. Thus, the eruption occurring here as the flows are arrested is very much like those that took place when the flows were held steady. Following the relaxation to its new equilibrium state, the configuration resembles the quasi-potential breakout state shown in Figure 5 (*middle*), except that the core field lines (*magenta*) are less sheared, resembling instead those in the immediate post-eruption state shown in Figure 6 (*bottom*). This simulated event, then, shows only a faint hint of reformation of the pre-eruption filament or sigmoid. Clearly, the ongoing footpoint motions play a crucially important part in the reformation process.

We have stressed in our presentation to this point the dynamical evolution of the magnetic field visualized from our simulation data, in particular the vital role of the high-coronal breakout reconnection in reconfiguring the connectivity of the field to the surface and enabling our homologous eruptions to occur. Because the actual coronal magnetic field can only rarely be measured directly, however, its global configuration must be inferred from surface measurements combined with field-extrapolation models. A realization of our scenario on the Sun would feature an equatorial bipolar active region, far removed from the polar caps, which gradually develops a filament and/or sigmoid along its PIL that eventually erupts. It could be questioned whether the remote, weak polar fields can have any significant influence on the occurrence of such an event. To address this issue, we repeated our original simulation, but with the polarity of the global background field reversed. In this case, whose initial state is shown in Figure 10, the northern hemisphere contains only negative-polarity flux concentrated near the pole and the equator, and the southern hemisphere only positive-polarity flux. That is, the solar magnetic field is strictly bipolar and consists of a single flux system. In recognition of this fundamental change, but to preserve the ability to distinguish the equatorial and polar arcade field lines, we have changed the color with which the polar lines are drawn from the previous quadrupolar case (*red*) to the current bipolar case (*light blue*). We applied the same footpoint motions as before, except for small changes in the parameters B_1, B_2 of the flow profile needed to compensate for the reversed background field.

The magnetic-field evolution in this simulation is both reassuringly similar to, and dramatically different from, that of our breakout configuration. We display the magnetic free energy (*solid* curve) and kinetic energy (*dotted* curve) for the bipolar case in Figure 11. The magnetic free energy rises monotonically throughout the evolution, although the rate of increase falls nearly to zero during a late, brief pause at about time $t = 4.25\times10^4$ s. This behavior contrasts sharply with that in the quadrupolar case, shown in Figure 4, in which the free energy suffers substantial drops at quasiperiodic intervals before resuming its overall upward trend a short time later. The kinetic energy in the bipolar case, on the other hand, exhibits quasiperiodic bursts that are qualitatively much like those obtained previously, with quantitatively similar timing and duration but far smaller amplitude. Whereas for our quadrupolar configuration, the peak kinetic energy was nearly 1.5×10^{29} ergs, or roughly 3% of the magnetic free energy, here the peak value is only about 2.5×10^{28} ergs, or about 0.5% of the free energy. These much smaller conversions of magnetic to kinetic energy allow the free energy to increase throughout the evolution of the bipolar configuration, although the late pause evident in the free energy coincides with the second burst of kinetic energy. The slope of the free energy curve also modulates slightly during the first burst.

The qualitative agreement between the kinetic energy curves in our quadrupolar and bipolar cases might suggest that the field evolution also should be qualitatively similar, though perhaps of lower intensity. This expectation is not borne out upon inspection of the developing field configuration, however. We have tracked the apex positions of the inner arcade field lines (*dark blue*) that are shown in Figure 10 and that are rooted at 10°, 13°, and 16° north latitude, within the stationary portions of the active region polarities. These lines are analogous to those drawn in Figure 8 (*left* panel) for our breakout configuration, which featured quasiperiodic episodes of steep rise, a break of the lines at high altitude, and their reformation at low altitude a short time thereafter. In sharp contrast, the bipolar arcade lines displayed here in Figure 12 simply undergo a quite steady, gradual rise in height as the magnetic shear and free energy accumulate over time. This slow evolution rather closely resembles that of the quadrupolar arcade field lines prior to reaching the threshold for eruption. Clearly, in the bipolar configuration the field lines above the equatorial polarity inversion line have not opened, and so there has been no ejection of the strongly sheared magnetic field residing there. There also has been no formation of the vertical (flare) current sheet above the PIL that we observed when the field opened in our quadrupolar simulation. At the latest time shown, the magnetic free energy is about 13% of the baseline potential-field energy (7.34×10^{31} ergs). This certainly is a relatively modest fraction of the total. However, our quadrupolar field is only slightly beyond that percentage (14.3%) at the latest time shown in Figure 4, and it seems well on its way to suffering its fourth homologous eruption.

These findings leave open the question of the dynamical nature of the kinetic energy bursts exhibited by our bipolar field. There is evidence that they are associated with episodes of magnetic reconnection occurring in the corona between the sheared fields of our active region and the unsheared background fields. We display the magnetic field at times $t = 2.25\times10^4$ s (*top*) and 3.25×10^4 s (*middle*) in Figure 13, from the usual east-limb remote (*left*) and southeast closeup (*right*) perspectives. The sheared-core field lines (*magenta*) of the active region exhibit the very elongated, flat shapes typical of our pre-eruptive breakout filament or sigmoid (cf. Fig. 6, *top right*). Other field lines (*cyan*) in Figure 13 initially were part of the background polar field (*light blue* in Figure 10), rooted at the central meridian at 25° north and south latitude (*top* and *middle* panels) and at 35° and 45° latitude (*middle* only). These lines have reconnected with sheared field lines rooted in the zone of footpoint motions in the active region, thereby acquiring shear themselves and reconfiguring the topology of the field at increasing distances from the active region as time passes. The very long jumps in the conjugate footpoint positions of these field lines suggest that they reconnected quite high in the corona. We observed similar reconnection events, between the strongly sheared filament field lines and their innermost overlying unsheared arcade lines, in our studies of filament formation, interaction, and merging in rectilinear geometries (DeVore & Antiochos 2000; DeVore et al. 2005; Aulanier et al. 2006). Here, the reconnection and ensuing relaxation of the field to a new, approximately force-free equilibrium appears to be responsible for the burst of kinetic energy centered at about time $t = 2.75\times10^4$ s. Later in the evolution, the volume of reconnecting field lines also spreads inward toward the core of the active region. At time $t = 4.75\times10^4$ s, as shown in Figure 13 (*bottom*), the strongly sheared-core field lines (*magenta*) have acquired a decidedly asymmetric configuration through reconnection events. The previously reconnected field lines (*cyan*) also have suffered additional reconnections, at least in some cases: note the wrapping of the two high-north-latitude field lines about each other at this latest time. In addition, the outermost equatorial arcade line (*blue*) is about to suffer a reconnection event with a sheared field line, and to end up rooted in the near foreground of the active-region polarity in the closeup view (*bottom left*). Because of this reconfiguration of its footpoint positions, we truncated its trajectory (*dashed* curve) at this time in Figure 12. The preceding reconnections and the resultant relaxation of the field geometry occur in conjunction with the second kinetic energy burst centered at about time $t = 4.375\times10^4$ s.

Our bipolar configuration accumulates substantial stress and free energy, reconnects a significant amount of flux at the perimeter of the sheared field, and develops a progressively more complex internal topology within the active region. Nevertheless, no eruptive opening of the field occurs over the duration of the simulation. As a consequence, we also find no evidence for reconnection occurring very low in the corona adjacent to the active region's PIL. Such flare-like reconnections take place only in our quadrupolar breakout simulation, and only while the overlying field is opening, so that a vertical current sheet is extant. Very clearly, the background

magnetic field of the Sun plays a critical, determinative role in the evolution of our active region. In the absence of breakout reconnection of the overlying restraining flux, which can happen only in a quadrupolar topology, we observe simply a gradual expansion of the whole configuration together with an increasingly complex and widespread entangling of the active-region and background magnetic fields.

4. DISCUSSION

We have simulated the nonlinear dynamical evolution of a simple, idealized, but fully three-dimensional magnetic configuration comprised of a bipolar active region imbedded in the global bipolar background field of the Sun. The magnetic field is energized by slow footpoint motions, imposed at the base of the simulation domain, that preserve the surface distribution of radial magnetic flux. There follows a long interval of gradual vertical expansion of the configuration as it accumulates magnetic shear and forms a highly stressed structure typical of solar filaments and/or X-ray sigmoids. In our magnetic breakout configuration, the active region and background fields are antiparallel, yielding a four-flux topology with separatrix surfaces and a null line at the boundaries between the flux systems. The slow stressing phase then culminates in the onset of reconnection across the current sheet that develops along the coronal null line. A brief interval of this breakout reconnection rapidly removes overlying field restraining the low-lying filament or sigmoid, and ushers in a second phase of strong outward acceleration to high velocity of the stressed flux. Accompanying this sudden rise is the formation of a vertical current sheet extending upward from the polarity inversion line of the active region, across which sheared field lines linking the active region to the background field reconnect with each other to produce new transequatorial-loop lines that follow the sheared-core field into the high corona. A third phase of the evolution ensues when the active-region flux above and within the sheared core is fully annihilated by the oppositely directed external background field, i.e., when the breakout reconnection ceases. The trailing transequatorial-loop field lines then sharply decelerate against the remainder of the Sun's background field in the high corona, and eventually come to rest there. Thus, our simulated eruption is confined (to the corona) rather than ejective (to interplanetary space) and, clearly, exhibits a three-phase acceleration profile of its disrupted, sheared flux. Following the eruption, much more mildly but finitely sheared field is left behind above the active region PIL. In principle, this field could either retain through the eruption, or promptly regain afterward, its cold filamentary or hot sigmoidal plasma, thus yielding the signatures of either a partial eruption or a full eruption with prompt reformation, respectively. The mid-coronal magnetic field, above the newly mildly sheared core and below the newly liberated transequatorial loop, suffers continuing reconnection across the vertical (flare) current sheet, reforming the coronal null and its surrounding breakout configuration and relaxing toward a potential state. If the slow footpoint motions persist, eventually the strongly sheared filament and/or sigmoid fields are fully restored. In time, the relentless buildup of magnetic stress and free energy triggers another eruption of the configuration that is essentially identical to the previous one. Thus, our simulation also exhibits homology, so long as the source of the replenishing free energy remains active.

So far as we are aware, ours is the first fully three-dimensional simulation to exhibit a prompt reformation of the source region's filamentary and/or sigmoidal character and, moreover, the first to demonstrate the homology of any coronal magnetic configuration via a sequence of self-consistently driven eruptions. The fundamental aspects of our simulation that allows these features to be realized are (1) our method of energizing the structure preserves the surface distribution of radial magnetic flux and (2) our stressed structure consists of a moderately sheared coronal arcade. In the aftermath of an eruption from any configuration in which most of the magnetic shear is ejected into the high corona or interplanetary space, the field in the low corona relaxes back toward a nearly potential state of much lower energy. In order for any subsequent eruption(s) to be homologous, therefore, the post-eruption state must resemble rather closely the pre-eruption state at some earlier time. We achieve this partly through our idealized B_r-preserving footpoint motions at the base, which ensure that the pre- and post-eruption potential states are not merely similar but identical. The remainder is accomplished by the flare reconnection and dynamical relaxation back to a nearly potential equilibrium state after each eruption, which are governed by the MHD equations. The stressed structure that develops from our

imposed footpoint motions is a moderately sheared arcade with a filament or sigmoid at its center and an increasingly potential field outside. When an eruption occurs, the most strongly sheared core flux and its overlying field – both more weakly sheared and unsheared – separate from the low-lying, weakly sheared flux. The former are ejected, and the last is left behind. Such a separation observationally implies either a partial eruption of the filament and/or sigmoid, or a full eruption with prompt reformation of at least part of the structure. Both are commonly observed on the Sun, and are relatively easy to realize from a sheared-arcade source such as ours. In contrast, it is difficult to envision how a monolithic flux rope of one or more turns could reform promptly in place after a full eruption that ejects the whole pre-event rope. Partial ejections of split flux ropes, in which one section of rope escapes the corona while a second section remains behind, have been simulated numerically by Gibson & Fan (2006) and Birn et al. (2006). Such events obviously require extensive reconnections to occur internal to the flux rope. Strictly speaking, in these cases the flux rope actually does not reform – part of it simply never leaves – and the final low-coronal configuration differs significantly from that at the outset. Whether homologous eruptions can occur in such a scenario has not yet been demonstrated.

There are a number of reported observations of homologous events involving filaments and/or sigmoids, flares, and CMEs. Morita et al. (2001) describe a series of three such events that occurred in the quadrupolar geometry of NOAA active region 7070 on 1992 February 21, 24, and 27 and were observed by *Yohkoh*. They found evidence for only modest changes in the photospheric flux distribution over the seven days of the sequence. Sterling & Moore (2001a,b) and collaborators (Sterling et al. 2001) used multiwavelength data to analyze three homologous eruptive flares in NOAA 8210 on 1998 May 1-2. They concluded that the events were fully consistent with, and showed distinctive signatures of, the breakout model for CMEs. The homology of the sequence was ascribed to the sustained emergence of new flux, and its cancellation with old flux, within the region. Nitta & Hudson (2001) also concluded that flux emergence and cancellation were responsible for a sequence of six recurrent eruptive flares in NOAA 9236 on 2000 November 24-26. Zhang & Wang (2002) focused on the role of moving magnetic features in triggering a subset of five of these events, while Takasaki et al. (2004) noted that the geometry of NOAA 9236 was multipolar and that each of the three flares on November 24 ejected a filament. Thus, it seems fair to say that all three of these homologous sequences occurred in a configuration consistent with breakout initiation. Although only NOAA 8210 has been analyzed with the breakout model in mind and referenced as such, the schematic diagram of a model (Takasaki et al. 2004) for NOAA 9236 is identical in all of its principal features to the more detailed diagram of a model for the earlier events (Sterling & Moore 2001a, b; Sterling et al. 2001).

The homologous sequences in both NOAA 8210 and 9236 were ascribed to ongoing flux emergence and cancellation in the respective active regions, which certainly is a plausible alternative to our B_r-preserving footpoint motions for generating a sustained series of eruptive flares. No evidence for such evolution has been cited in the case of NOAA 7070, however, so that its energization by motions similar to those in our model offers a plausible account of its homologous behavior. Moreover, Règnier & Canfield (2006) performed and analyzed force-free extrapolations of the magnetic fields of NOAA 8210 over an interval that includes the first of the homologous flares studied by Sterling et al. They concluded that NOAA 8210 was energized more by the rapid, organized motions of its flux across the surface, in particular a rotation of one of its sunspots, than by the emergence of new flux from below, and that those motions principally powered the region's eruptive flares. As we noted above, Zhang & Wang (2002) also emphasized the possible role of moving magnetic features in triggering the homologous events in NOAA 9236. More recently, Zhang et al. (2008) associated persistent sunspot rotations in the complex active region NOAA 10486 with a pair of homologous eruptive flares that occurred two days apart during the Halloween storms of late October 2003. In other studies of nonhomologous eruptive flares, Tian & Alexander (2006) observed persistent sunspot rotation in NOAA 9684 prior to ejection of a filament, sigmoid, and CME. Brown et al. (2003) analyzed *TRACE* data to determine the rotation rates of seven sunspots, six of which gave rise to eruptive flares including the spectacular Bastille Day event from NOAA 9077 on 2000 July 14, with total rotation angles and durations reaching 200° and five days, respectively.

Thus, there is much persuasive evidence that footpoint motions of active region magnetic fields play an important, even decisive, role in energizing the overlying corona prior to eruptive flares. Multipolar active regions that are potentially vulnerable to breakout initiation of eruptions also seem to host most homologous flare sequences, which regularly exhibit more or less prompt reformation of their embedded filaments and/or sigmoids. These findings are very supportive of the theoretical model that we have proposed and investigated numerically in this paper. However, we emphasize that our simple, highly idealized experiment is not meant to model any particular observed event; it is too far removed from realistic solar conditions. For example, we have argued simply on the basis of magnetic field line geometry and detailed one-dimensional modeling (Karpen et al. 2006) that our initially formed, and post-eruptively reformed, sheared structures could plausibly host cold filaments if heated near the footpoints of the field lines (or, alternatively, hot sigmoids if heated near the loop tops). A definitive demonstration that this assertion is correct would require a far more detailed thermal model of the plasma than ours, including coronal heating, thermal conduction, and radiative losses. Such a model also might capture and redistribute appropriately the heating due to numerical resistivity that is lost from the adiabatic temperature equation. Despite these limitations of our present simulation, however, its principal features are quite encouragingly consistent with the observational studies cited above.

A third facet of the simulation results that is commonly observed in filament eruptions is the multiphase acceleration profile of the sheared, disrupted flux. We find a long interval of slow upward expansion during the energization phase that culminates in the onset and completion of breakout reconnection of the overlying, restraining field; there follows a short interval of fast outward acceleration of the sheared-core flux and of newly formed transequatorial-loop field lines; and the event concludes with a short interval of strong deceleration to rest of the transequatorial loop in the high corona. Our previous work on axisymmetric breakout configurations (Antiochos et al. 1999; MacNeice et al. 2004) showed analogous features in the acceleration profiles, although (1) the special symmetry in those cases leads to the formation of flux ropes disconnected from the solar surface, rather than rooted transequatorial loops as in the present fully three-dimensional geometry, and (2) the flux rope was ejected from the Sun rather than being confined to the high corona. Initially (Antiochos et al. 1999), we were able to follow the evolution of the field only into the early portion of the second phase of the event, so that we clearly saw only the abrupt transition from long/slow to short/fast acceleration as energization gave way to eruption. Subsequently (MacNeice et al. 2004), using a more robust numerical model exploiting adaptive mesh refinement, we were able to follow the event sequence all of the way through ejection of a flux rope into the heliosphere. In that simulation, we found that a third phase of enhanced outward acceleration accompanied the onset of flare reconnection below the rising sheared-core field, which disconnected flux from the surface and ejected it into interplanetary space. In our present simulation of a confined eruption, flare reconnection again sets in at the beginning of the third phase of acceleration, but here any liberating effect on the rapidly rising sheared flux is overwhelmed by the deceleration associated with the tension of the overlying, high-coronal field lines. In all cases, therefore, we have found that phase two consists of an ideal expansion of the stressed flux out of the low corona at the Alfvén speed, following the essential completion of the breakout reconnection at the end of phase one, and preceding the onset of flare reconnection at the beginning of phase three.

Several well-observed eruptions of filaments or X-ray sigmoids have been analyzed to reveal both two-phase (Sterling & Moore 2004a,b) and three-phase (Ji et al. 2003; Li et al. 2005; Bong et al. 2006) acceleration profiles of the disrupted structures. All of these events were judged to have occurred in breakout-susceptible, multipolar geometries. Sterling & Moore and Ji et al. cite evidence for signatures of breakout reconnection in the events that they studied, as do Gary & Moore (2004) in their independent investigation of the event reported by Li et al. Bong et al. conclude that their observations contradict the breakout model because the first interval of strong outward acceleration (our phase two) precedes both the opening of the coronal field as observed coronagraphically and the onset of still faster radial acceleration (our phase three). Our simulation shows clearly that the opening of the coronal field (or at least its greatest distention, since our eruption is confined) occurs *after* the breakout reconnection is already complete, and the flare reconnection is commencing below. Indeed, in the observations described by Bong et al., flare emission onset coincides with the transition to a final

phase of enhanced outward acceleration, just as we found in MacNeice et al. (2004). Thus, we would interpret their sequence of events as being fully consistent with our current and past simulations of breakout eruptions.

A significant point of departure from our previous axisymmetric simulations of breakout (MacNeice et al. 2004; Phillips et al. 2005) is that those eruptions were ejective, whereas the fully three-dimensional eruption we have described here is confined. Thus, this paper also constitutes the first demonstration of confined solar eruptions via magnetic breakout. Observational studies of confined (or 'failed') eruptions have shown that their only certain signature is the absence of an associated coronal mass ejection (Moore et al. 2001; Choudhary & Moore 2003). Some of the just-cited confined events do not exhibit flare emissions, while others do. This latter class includes the confined filament eruption in a breakout configuration analyzed by Ji et al. (2003). Our simulation shows clear evidence for flare reconnection, and so is qualitatively fully consistent with their data and interpretation. Alexander et al. (2006) have reexamined the data for this event and conclude that an ideal kink instability may be responsible for the eruption, while Williams et al. (2005) draw the same conclusion for an ejective filament eruption from a breakout-susceptible multipolar source. Both investigations cite the simulations of flux ropes subject to a growing kink mode by Török & Kliem (2005). Our sheared-core field lines are well below the threshold for kink instability, however, possessing only about half a turn from end to end, so that mechanism is not in play in our simulation. A key theoretical issue that is unresolved is how a highly twisted, strongly kink-unstable flux rope could be created in the corona in the first place. A super-Alfvénic twisting to attain that state would seem to be required, since the magnetohydrodynamic evolution should accommodate typically slow photospheric motions to find an accessible, stable equilibrium in the corona. Other ideal-MHD instabilities, such as the torus instability at smaller twist (Kliem & Török 2006; Isenberg & Forbes 2007), likewise would seem to require that the unstable equilibrium be created on a shorter time scale than the resultant motions can relax it away. Ideal, catastrophic failures of equilibrium have been shown to occur in certain configurations and to induce fast motions on the Alfvén time scale (e.g., Forbes et al. 1994; Zhang et al. 2005; Zhang & Wang 2007). However, there is no evidence that such a failure occurs in our simulation: the sheared-core flux moves upward smoothly, accompanying rather than preceding the onset of significant breakout reconnection in the corona above it.

In their analysis of several well-observed eruptions, both ejective and confined, Moore et al. (2001) assert that the source regions of their events are simple bipolar configurations with no observable influences of either neighboring active regions or of the Sun's global background field. The eruptions are described as resulting from tether-cutting reconnection (Sturrock 1989; Moore & Roumeliotis 1992) that weakens the restraining fields above and around the strongly sheared core flux, which then is ejected or disrupted in the events. Our model configuration consists of an isolated bipolar active region centered on the equator, embedded in the Sun's global background field. When we aligned the magnetic moments of our active region and background field, so that the model Sun was strictly bipolar, we observed tether-cutting-like reconnections between the sheared-core flux and the unsheared flux outside at the perimeter between them. However, no eruption occurred: the restraining arcade field above the sheared core lifted upward, but did not open to allow the filament and/or sigmoid to escape from below. This result is in agreement with the conjecture of Aly (1991) and Sturrock (1991) that the ideal force-free equilibrium state of maximum energy is the open configuration. Under their conjecture, the outcome of our slowly driven numerical experiment should be a closed equilibrium field that expands and opens gradually as its energy builds toward the upper-bound energy of the open state. This is fully consistent with our findings, in which the bipolar case remains in a quiescent near-equilibrium state with a magnetic free energy at which the companion multipolar case already has shed three filaments in successive eruptions. Our results also concur in this important respect with those of Amari et al. (2007; see also Amari et al. 2000), who found that their own bipolar configuration entered its rapid expansion phase only as the total magnetic energy approached that of the associated fully open state. Meanwhile, their multipolar case began to erupt at the substantially lower energy of the state in which only the core active-region flux opens, with the rest of the configuration, including essentially all of the background field, remaining closed. We discovered that the latter threshold also was the critical point for eruption onset in our previous breakout simulations (Antiochos et al. 1999; MacNeice et al. 2004), by constructing and analyzing the associated partially open axisymmetric states

(DeVore & Antiochos 2005). There seems to be a developing concordance toward the idea that the critical criterion for eruption onset is the accumulation of sufficient magnetic free energy to power an ideal opening of the participating configuration. It will be very interesting to see how that conjecture holds up under further testing, by ourselves and others.

As stated earlier in the paper, we found in our simulation that the strongly sheared core flux of our active region filament suffers breakout reconnection during its rapid rise through the corona. Only the transequatorial loops that are formed during the eruption, and trail the filament, survive this rise to find a new equilibrium state high in the atmosphere. This sequence bears an intriguing resemblance to the development of an ejective filament eruption from a breakout geometry analyzed by Li et al. (2005), which we referenced above, except that their filament fields seem to have survived the transit through the corona and gradually faded from view. The fascinating aspect to that event is an EUV helix that is seen to trail the filament on its path from the low corona. Li et al. conclude that the helix was formed by reconnection occurring just above the polarity inversion line where the filament resided. It seems plausible that their ejected EUV helix originated in flare reconnections like those that formed the transequatorial-loop field lines in our simulation. Further assessment of this possibility awaits the analysis of fully ejective eruptions from a variant of our current configuration (DeVore et al. 2008). Meanwhile, in confined events such as those simulated here, the magnetic helicity resident on the filament and/or sigmoid field lines disrupted by the event must be transferred to higher-lying field lines rooted farther away from the source. This implication of helicity conservation in confined eruptions could be tested by high-resolution, multispectral observations such as those forthcoming from the Solar Dynamics Observatory.

We appreciate stimulating discussions of three-dimensional breakout with Benjamin J. Lynch, of flare reconnection and CME acceleration with Terry G. Forbes, and of our initial results on this problem with other members of the NASA Living With a Star team on the CME/ICME connection led by Zoran Mikić. Ravi Ramamurti kindly assisted us with the preparation of the computer animation. We thank our anonymous referee for cogent criticisms that led to improvements in the paper. C.R.D. acknowledges with gratitude a lifetime of support and encouragement from Carl T. DeVore. Generous grants of computer time were provided by the DoD High Performance Computing Modernization Program at the NRL-DC resource center to perform the numerical simulations. Our research was supported by NASA, ONR, and the NSF SHINE program.

REFERENCES

Alexander, D., Liu, R., & Gilbert, H. R. 2006, ApJ, 653, 719
Aly, J. J. 1991, ApJ, 375, L61
Amari, T., Aly, J. J., Mikic, Z., & Linker, J. A. 2007, ApJ, 671, L189
Amari, T., Luciani, J. F., Mikic, Z., & Linker, J. A. 2000, ApJ, 529, L49
Antiochos, S. K. 1998, ApJ, 502, L181
Antiochos, S. K., DeVore, C. R., & Klimchuk, J. A. 1999, ApJ, 510, 485
Aulanier, G., DeVore, C. R., & Antiochos, S. K. 2006, ApJ, 646, 1349
Birn, J., Forbes, T. G., & Hesse, M. 2006, ApJ, 645, 732
Bong, S. C., Moon, Y.-J., Cho, K. S., Kim, Y. H., Park, Y. D., & Choe, G. S. 2006, ApJ, 636, L169
Brown, D. S., Nightingale, R. W., Alexander, D., Schrijver, C. J., Metcalf, T. R., Shine, R. A., Title, A. M., & Wolfson, C. J. 2003, Sol. Phys., 216, 79
Choudhary, D. P., & Moore, R. L. 2003, Geophys. Res. Lett., 30, Art. 2107
Crooker, N., Joselyn, J. A., & Feynman, J. 1997, Coronal Mass Ejections (Washington DC: AGU)
DeVore, C. R., & Antiochos, S. K. 2000, ApJ, 539, 954
---. 2005, ApJ, 628, 1031
DeVore, C. R., Antiochos, S. K., & Aulanier, G. 2005, ApJ, 629, 1122
DeVore, C. R., Antiochos, S. K., Lynch, B. J., MacNeice, P. J., & Olson, K. M. 2008, ApJ, in preparation
Duvall, T. L., Scherrer, P. H., Svalgaard, L., & Wilcox, J. M. 1979, Sol. Phys., 61, 233

Forbes, T. G. 2000, J. Geophys. Res., 105, 23153
Forbes, T. G., Linker, J. A., Chen, J., Cid, C., Kota, J., Lee, M. A., Mann, G., Mikic, Z., Potgieter, M. S., Schmidt, J. M., Siscoe, G. L., Vainio, R., Antiochos, S. K., & Riley, P. 2006, Space Sci. Rev., 123, 251
Forbes, T. G., Priest, E. R., & Isenberg, P. A. 1994, Sol. Phys., 150, 245
Gary, G. A., & Moore, R. L. 2004, ApJ, 611, 545
Gibson, S. E., & Fan, Y. 2006, ApJ, 637, L65
Gopalswamy, N., Mewaldt, R., & Torsti, J. 2006, Solar Eruptions and Energetic Particles (Washington DC: AGU)
Isenberg, P. A., & Forbes, T. G. 2007, ApJ, 670, 1453
Ji, H., Wang, H., Schmahl, E. J., Moon, Y.-J., & Jiang, Y. 2003, ApJ, 595, L135
Karpen, J. T., Antiochos, S. K., & DeVore, C. R. 2006, ApJ, 637, 531
Kliem, B., & Török, T. 2006, Phys. Rev. Lett., 96, 255002
Klimchuk, J. A. 2001, in Space Weather, ed. P. Song, H. J. Singer, & G. L. Siscoe (Washington DC: AGU), 143
Kunow, H., Crooker, N. U., Linker, J. A., Schwenn, R., & von Steiger, R. 2006, Coronal Mass Ejections (Dordrecht: Springer)
Li, J., Mickey, D. L., & LaBonte, B. J. 2005, ApJ, 620, 1092
Lin, J., Soon, W., & Baliunas, S. L. 2003, New Astron. Rev., 47, 53
Lynch, B. J., Antiochos, S. K., DeVore, C. R., & Zurbuchen, T. H. 2005, in Solar Wind 11, ESA Conf. Proceed. SP-592 (ESA), 297
MacNeice, P., Antiochos, S. K., Phillips, A., Spicer, D. S., DeVore, C. R., & Olson, K. 2004, ApJ, 614, 1028
Mikic, Z., & Lee, M. A. 2006, Space Sci. Rev., 123, 57
Moore, R. L., Sterling, A. C., Hudson, H. S., & Lemen, J. R. 2001, ApJ, 552, 833
Moore, R. M., & Roumeliotis, G. 1992, in Eruptive Solar Flares, ed. Z. Svestka, B. V. Jackson, & M. E. Machado (New York: Springer), 69
Morita, S., Uchida, Y., Hirose, S., Uemura, S., & Yamaguchi, T. 2001, Sol. Phys., 200, 137
Nitta, N. V., & Hudson, H. S. 2001, Geophys. Res. Lett., 28, 3801
Phillips, A., MacNeice, P., & Antiochos, S. K. 2005, ApJ, 624, L129
Règnier, S., & Canfield, R. C. 2006, A&A, 451, 319
Song, P., Singer, H. J., & Siscoe, G. L. 2001, Space Weather (Washington DC: AGU)
Sterling, A. C., & Moore, R. L. 2001a, ApJ, 560, 1045
---. 2001b, J. Geophys. Res., 106, 25227
---. 2004a, ApJ, 602, 1024
---. 2004b, ApJ, 613, 1221
Sterling, A. C., Moore, R. L., Qiu, J., & Wang, H. 2001, ApJ, 561, 1116
Sturrock, P. A. 1989, Sol. Phys., 121, 387
---. 1991, ApJ, 380, 655
Takasaki, H., Asai, A., Kiyohara, J., Shimojo, M., Terasawa, T., Takei, Y., & Shibata, K. 2004, ApJ, 613, 592
Tian, L., & Alexander, D. 2006, Sol. Phys., 233, 29
Török, T., & Kliem, B. 2005, ApJ, 630, L97
Williams, D. R., Török, T., Démoulin, P., van Driel-Gesztelyi, L., & Kliem, B. 2005, ApJ, 628, L163
Zhang, J., & Wang, J. 2002, ApJ, 566, L117
Zhang, Y., Liu, J., & Zhang, H. 2008, Sol. Phys., 247, 39
Zhang, Y. Z., Hu, Y. Q., & Wang, J. X. 2005, ApJ, 626, 1096
Zhang, Y. Z., & Wang, J. X. 2007, ApJ, 663, 592

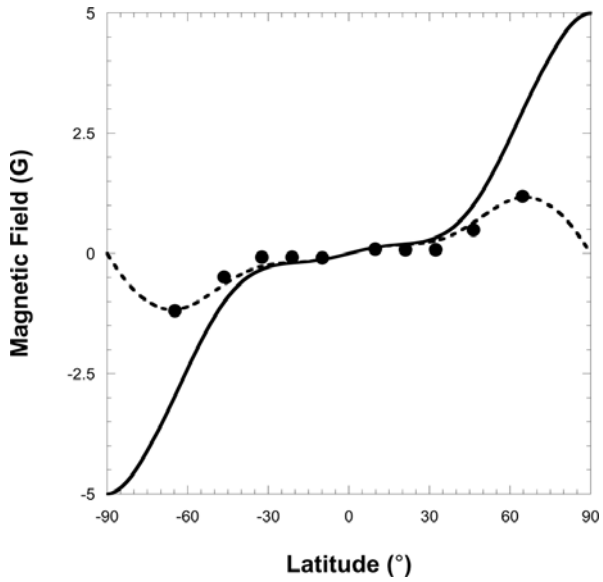

Figure 1. Assumed axisymmetric background radial magnetic field (*solid* curve) and its line-of-sight projection (*dashed* curve); Wilcox Solar Observatory line-of-sight measured values (*filled circles*) are from Duvall et al. (1979).

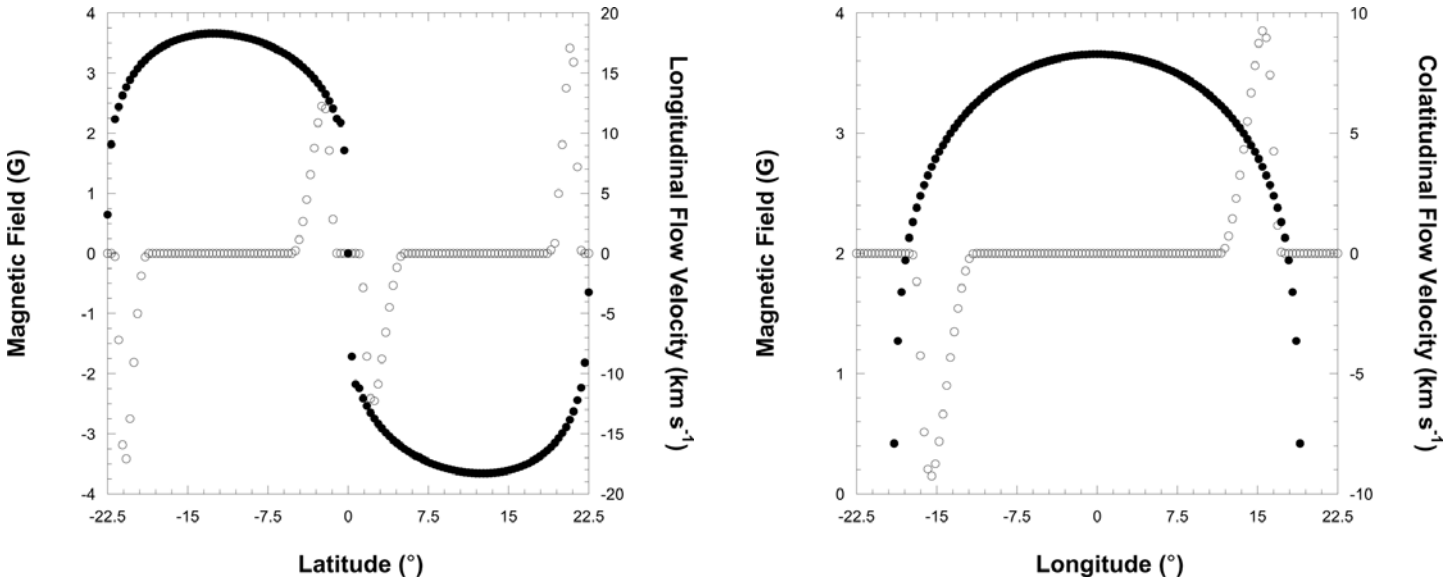

Figure 2. Radial magnetic field (*filled circles*) in the active region versus latitude at central meridian (*left*) and versus longitude at the southern latitude of peak field strength (*right*); imposed flow velocities (*open circles*) in the longitudinal (*left*) and colatitudinal (*right*) directions are shown at the same positions. Each symbol on the graphs corresponds to a point on the simulation grid.

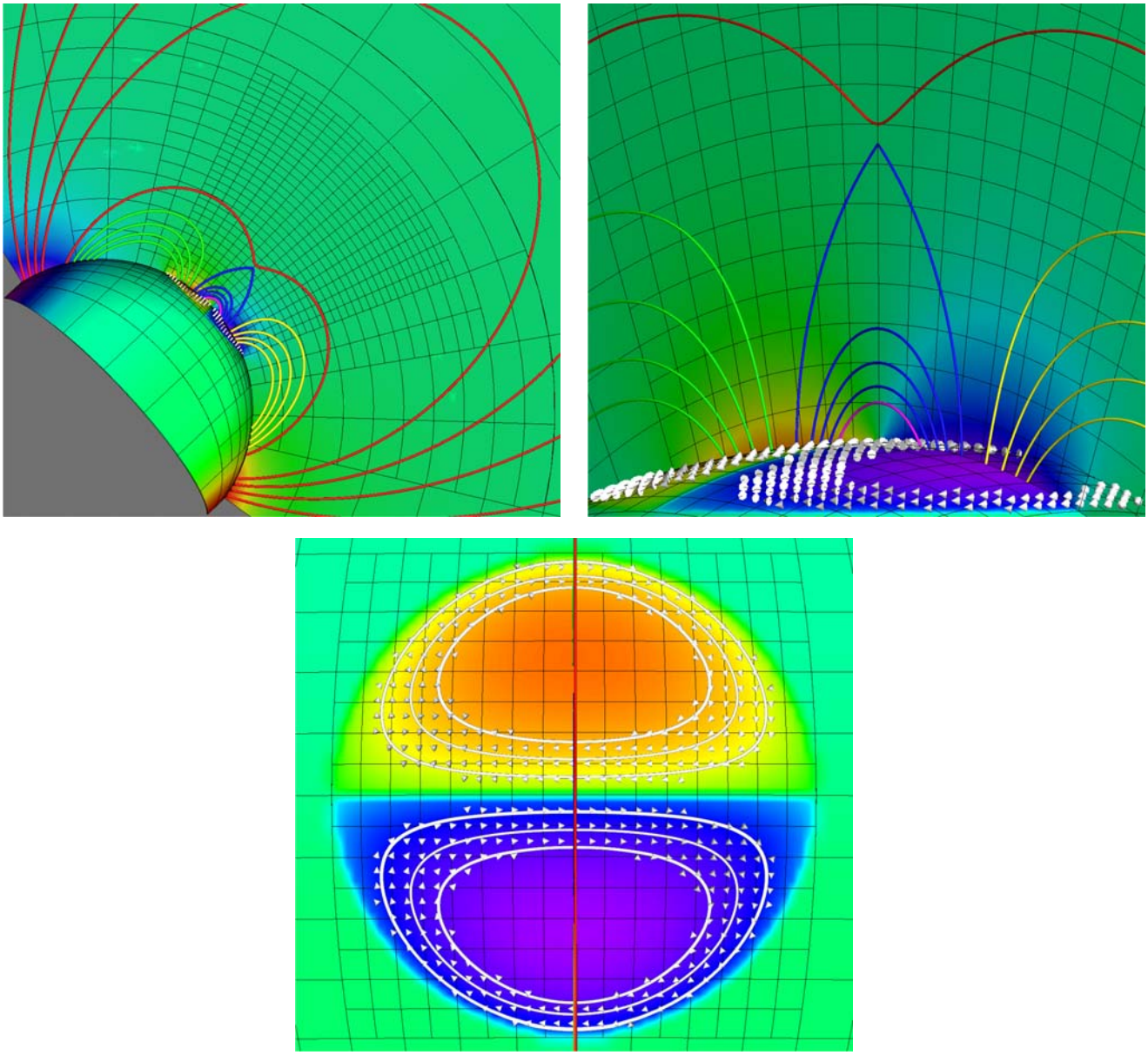

Figure 3. Global (*top left*), closeup (*top right*), and overhead (*bottom*) views of the *ARMS* adaptive grid lines (*black*), surface flow arrowheads and streamlines (*white*), radial magnetic field magnitude and sign (*red* to *blue* surface shading of negative to positive values), and selected magnetic field lines showing the initial potential state of the breakout configuration. Field line color identifies the flux system to which each line belongs (equatorial: *blue*; polar: *red*; north midlatitude: *green*; south midlatitude: *yellow*) and distinguishes the sheared filament-channel field lines of the equatorial system (*magenta*) and the transequatorial-loop field lines of the polar system (*cyan* in subsequent figures) formed during the eruptions.

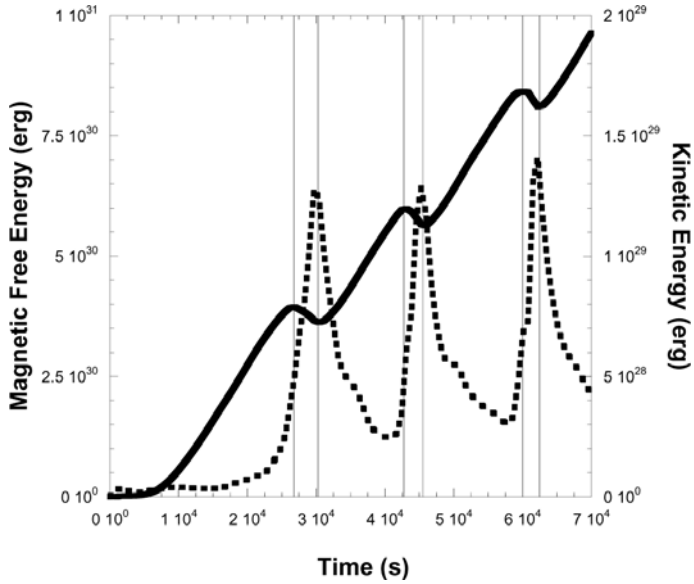

Figure 4. Changes in magnetic (*solid* curve) and kinetic (*dotted* curve) energies from the initial equilibrium state. Thin vertical lines in both panels mark the local extrema in the magnetic free energy.

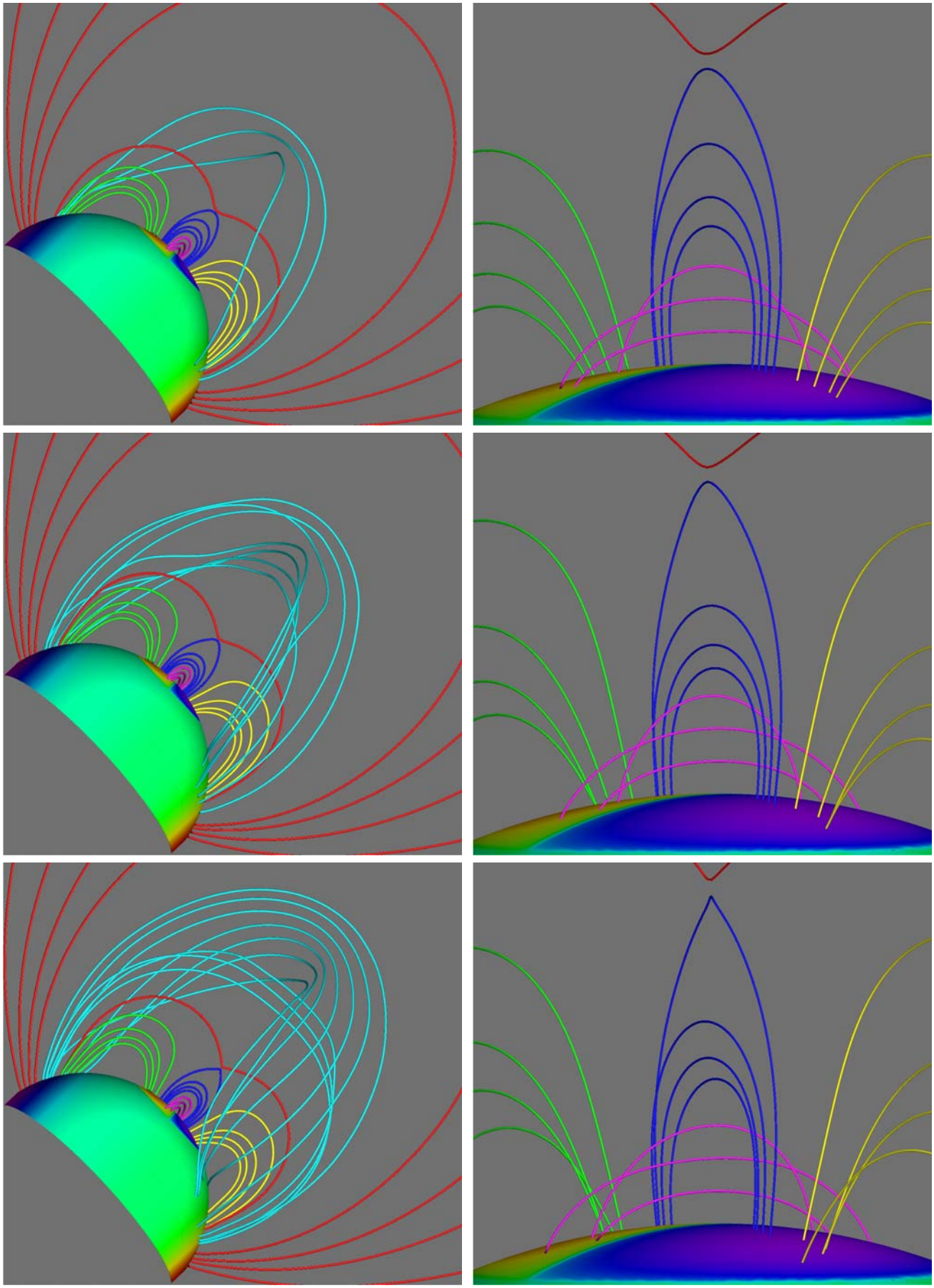

Figure 5. Global (*left*) and closeup (*right*) views of the post-eruption magnetic fields following each of three homologous events, at times $t = 3.625 \times 10^4$ s (*top*), 5.25×10^4 s (*middle*), and 7.0×10^4 s (*bottom*).

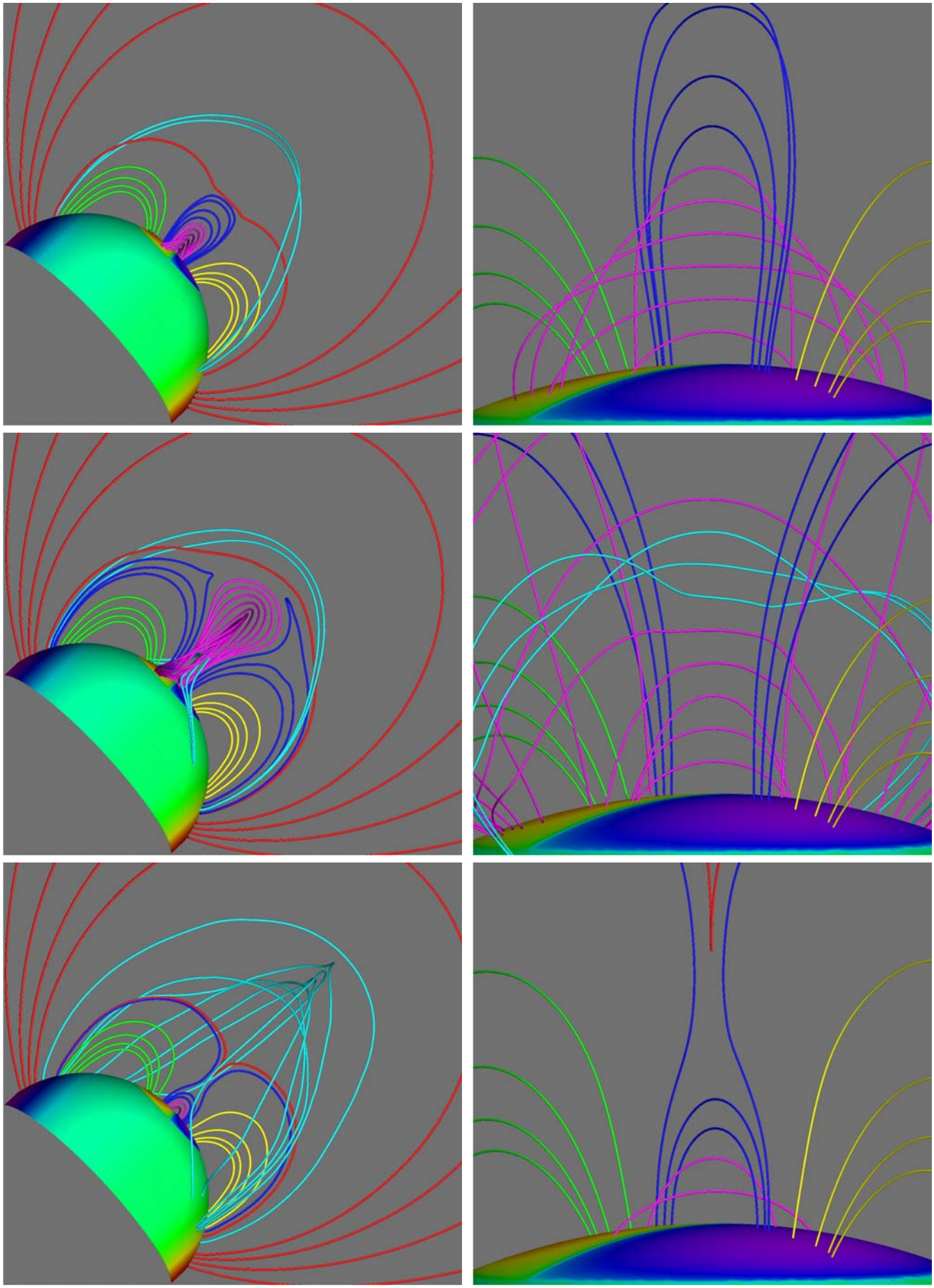

Figure 6. Global (*left*) and closeup (*right*) views of magnetic fields during the second of three homologous eruptions, at times $t = 4.125 \times 10^4$ s (*top*), 4.375×10^4 s (*middle*), and 4.625×10^4 s (*bottom*).

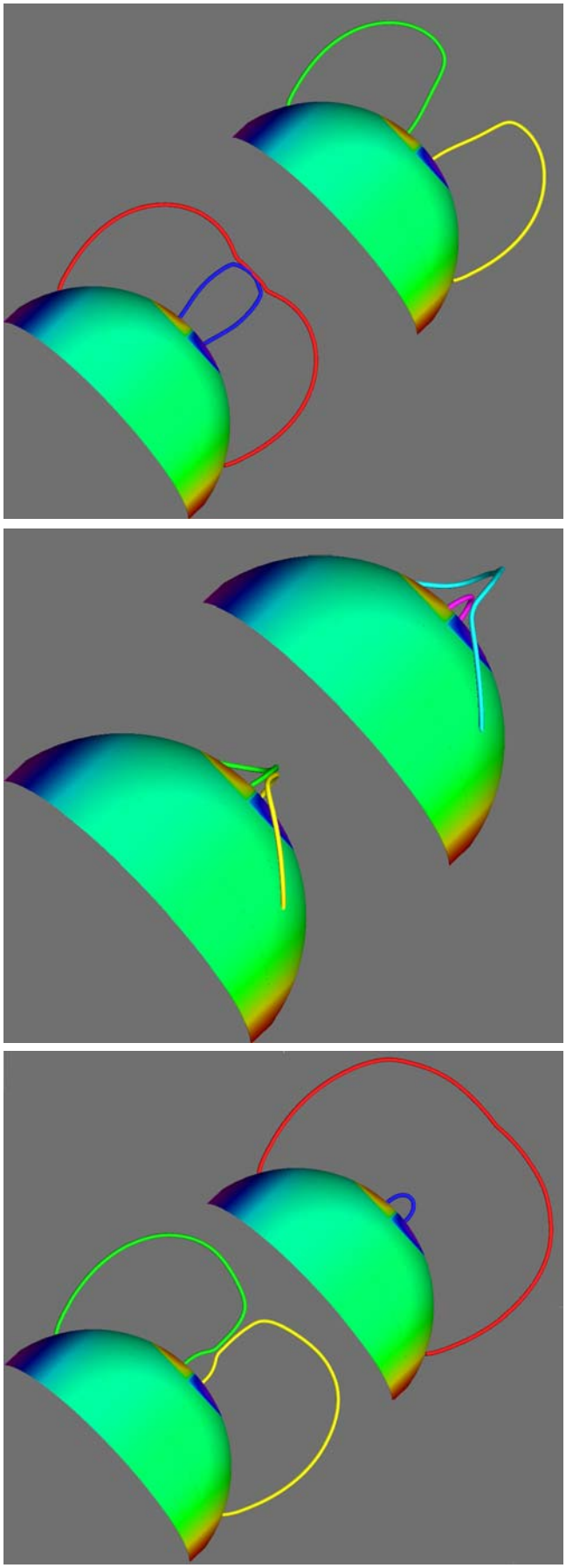

Figure 7. Pre- (*lower left* in each panel) and post-reconnection (*upper right*) magnetic field lines, illustrating the breakout (early eruption: *top*) and flare (mid eruption: *middle*; late eruption: *bottom*) reconnection processes.

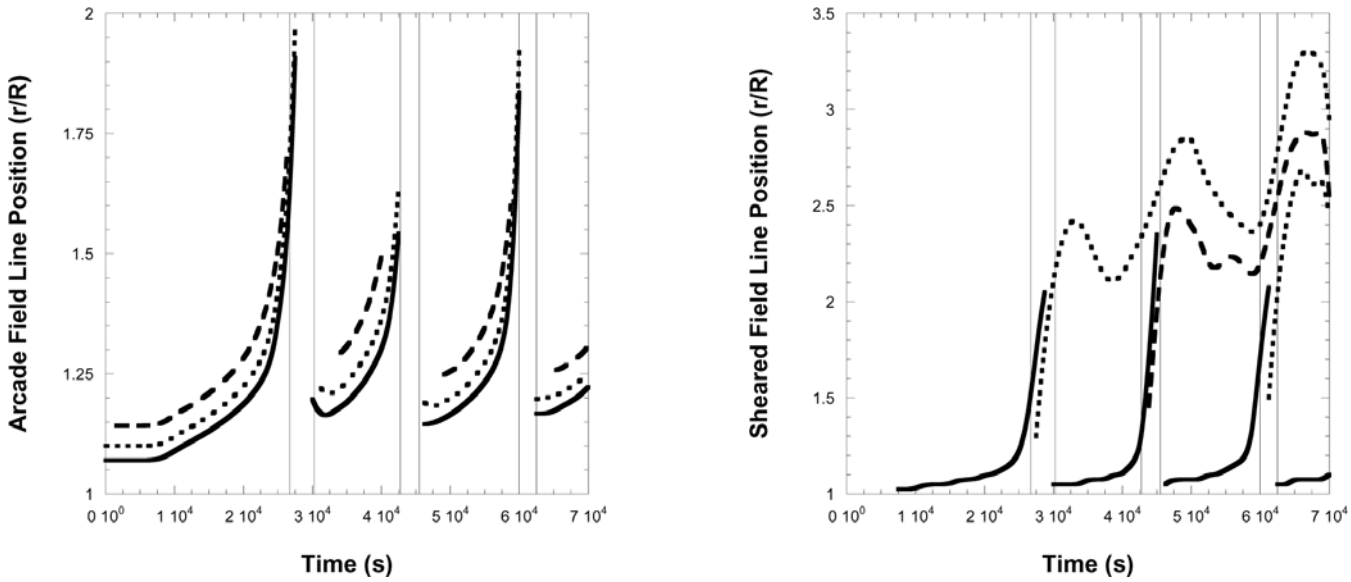

Figure 8. *Left*: Apex positions of field lines of the unsheared equatorial arcade overlying the sheared flux, for the configuration shown in Figure 3. Their footpoints are at north latitudes 5.5° (*solid* curves), 6.5° (*dotted* curves), and 7.5° (*dashed* curves). *Right*: Apex positions of sheared-core field lines (*solid* curves) and sheared transequatorial-loop field lines formed by flare reconnection during the eruptions (*dotted* and *dashed* curves). Note the change in the vertical scale at right. Thin vertical lines in both panels mark the local extrema in the magnetic free energy shown in Figure 4.

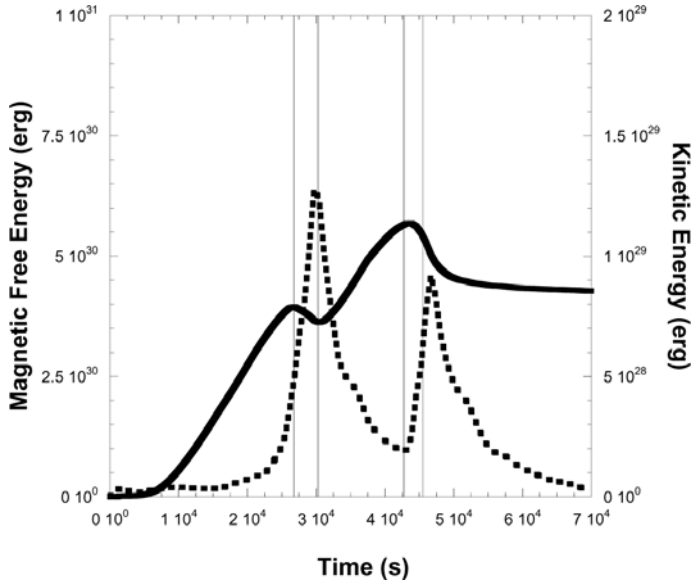

Figure 9. Changes in magnetic and kinetic energies from the initial equilibrium state, as in Figure 4, when the imposed footpoint motions are smoothly arrested between times $t = 3.75\times10^4$ s and 4.75×10^4 s, approaching the onset of the second eruption.

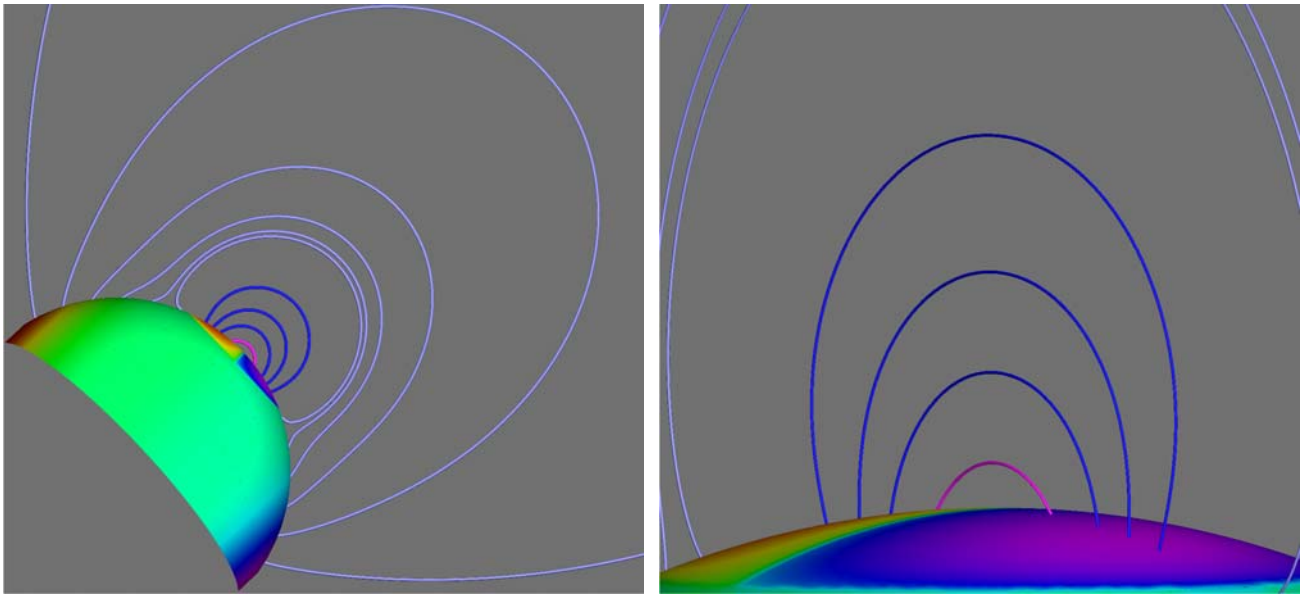

Figure 10. Global (*left*) and closeup (*right*) views of the initial magnetic configuration when the global background field is reversed from its orientation in Figure 3, so that the flux distribution is strictly bipolar. Colors distinguish field lines in the sheared core (*magenta*), the unsheared equatorial arcade (*dark blue*), and the unsheared polar arcade (*light blue*). The imposed motions are essentially identical to those in Figure 3's bottom panel.

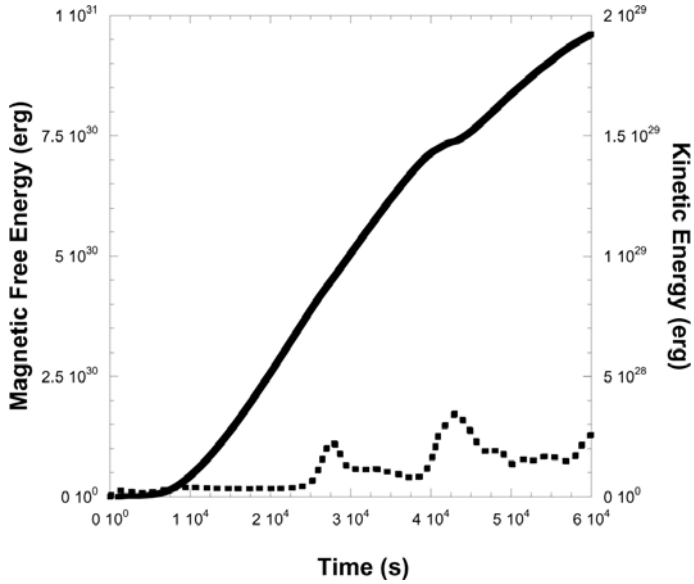

Figure 11. Changes in magnetic and kinetic energies from the initial equilibrium of the bipolar configuration shown in Figure 10, for comparison with the energy changes (Fig. 4) in the quadrupolar configuration (Fig. 3).

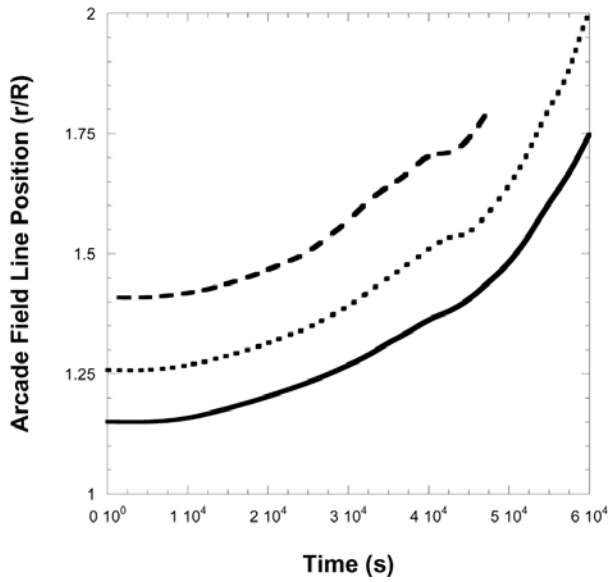

Figure 12. Apex positions of field lines of the unsheared equatorial arcade overlying the sheared flux, for the bipolar configuration shown in Figure 10. Their footpoints are at north latitudes 10° (*solid* curve), 13° (*dotted* curve), and 16° (*dashed* curve). Compare these with the apex positions (Fig. 8, *left*) for the quadrupolar configuration (Fig. 3).

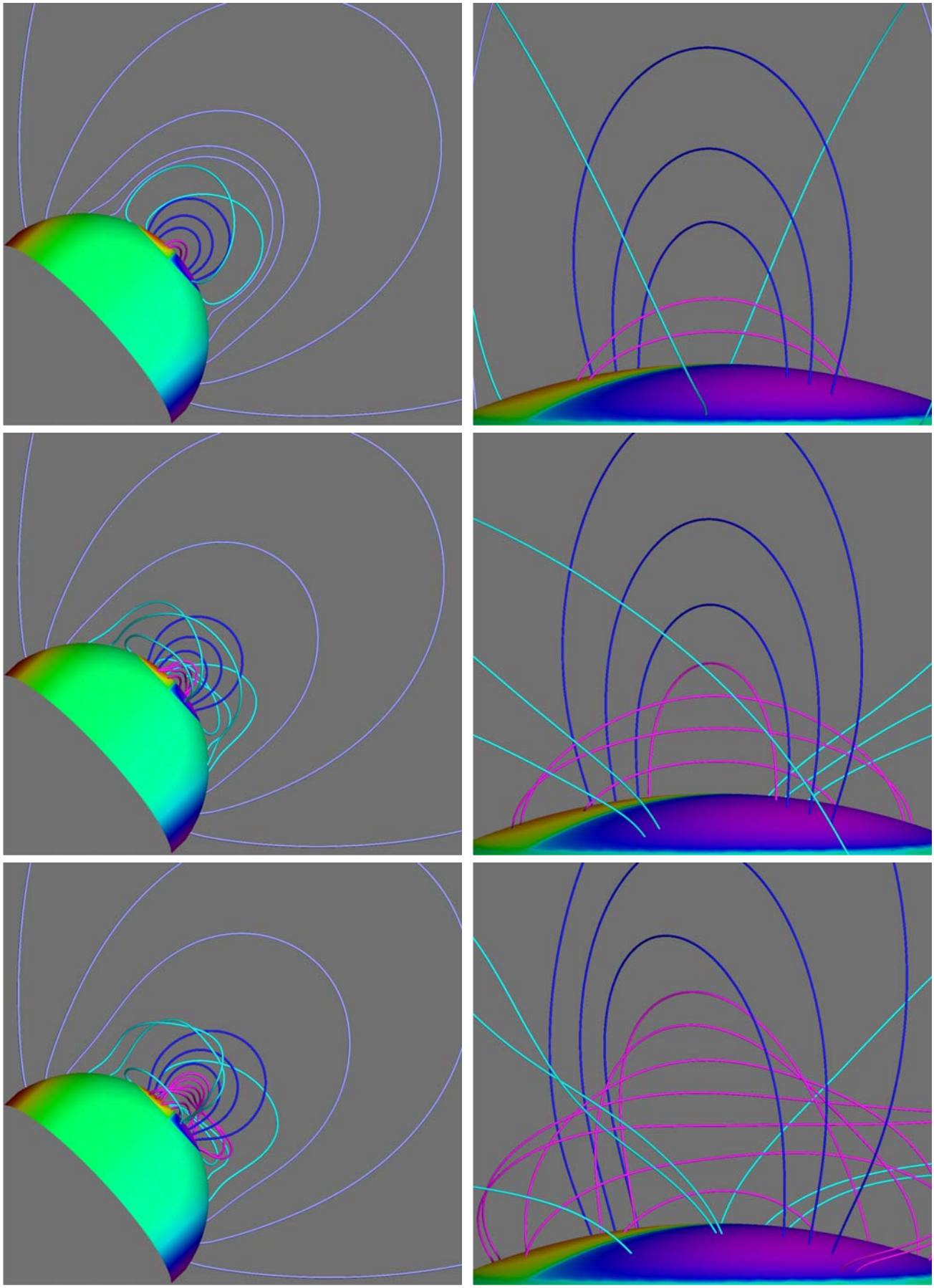

Figure 13. Global (*left*) and closeup (*right*) views of magnetic fields during the expansion of the bipolar configuration shown in Figure 10, at times $t = 2.25 \times 10^4$ s (*top*), 3.25×10^4 s (*middle*), and 4.75×10^4 s (*bottom*).